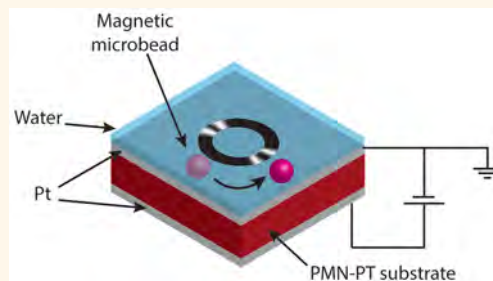


# Electrically Driven Magnetic Domain Wall Rotation in Multiferroic Heterostructures to Manipulate Suspended On-Chip Magnetic Particles

Hyunmin Sohn,<sup>†</sup> Mark E. Nowakowski,<sup>§</sup> Cheng-yen Liang,<sup>‡</sup> Joshua L. Hockel,<sup>‡</sup> Kyle Wetzlar,<sup>‡</sup> Scott Keller,<sup>‡</sup> Brenda M. McLellan,<sup>||</sup> Matthew A. Marcus,<sup>⊥</sup> Andrew Doran,<sup>⊥</sup> Anthony Young,<sup>⊥</sup> Mathias Kläui,<sup>#</sup> Gregory P. Carman,<sup>‡</sup> Jeffrey Bokor,<sup>§</sup> and Robert N. Candler<sup>\*,†,∇</sup>

<sup>†</sup>Department of Electrical Engineering and <sup>‡</sup>Department of Mechanical and Aerospace Engineering, University of California, Los Angeles, California 90095, United States, <sup>§</sup>Department of Electrical Engineering and Computer Sciences, University of California, Berkeley, California 94720, United States, <sup>||</sup>Department of Physics, NYU Polytechnic School of Engineering, New York, New York 11201, United States, <sup>⊥</sup>Advanced Light Source, Lawrence Berkeley National Laboratory, Berkeley, California 94720, United States, <sup>#</sup>Institute of Physics, Johannes Gutenberg University, 55128 Mainz, Germany, and <sup>∇</sup>California NanoSystems Institute, Los Angeles, California 90095, United States. H.S. and M.E.N. contributed equally to this work.

**ABSTRACT** In this work, we experimentally demonstrate deterministic electrically driven, strain-mediated domain wall (DW) rotation in ferromagnetic Ni rings fabricated on piezoelectric  $[\text{Pb}(\text{Mg}_{1/3}\text{Nb}_{2/3})\text{O}_3]_{0.66}-[\text{PbTiO}_3]_{0.34}$  (PMN–PT) substrates. While simultaneously imaging the Ni rings with X-ray magnetic circular dichroism photo-emission electron microscopy, an electric field is applied across the PMN–PT substrate that induces strain in the ring structures, driving DW rotation around the ring toward the dominant PMN–PT strain axis by the inverse magnetostriction effect. The DW rotation we observe is analytically predicted using a fully coupled micromagnetic/ elastodynamic multiphysics simulation, which verifies that the experimental behavior is caused by the electrically generated strain in this multiferroic system. Finally, this DW rotation is used to capture and manipulate micrometer-scale magnetic beads in a fluidic environment to demonstrate a proof-of-concept energy-efficient pathway for multiferroic-based lab-on-a-chip applications.



**KEYWORDS:** multiferroics · lab-on-a-chip · energy-efficient magnetic technology · micromagnetic/elastodynamic coupled model · electrically driven magnetic domain wall motion

Controlling the orientation and position of magnetic domains and their domain walls (DWs) has historically required applying external magnetic fields generated by currents flowing through wires. However, recent research motivated by the development of energy-efficient technologies has investigated electric field<sup>1–5</sup> and spin-torque-based methods<sup>6</sup> capable of manipulating the magnetic properties of on-chip magnets without external magnetic fields. Although previous research efforts have been focused on computer-based applications such as next-generation memory devices<sup>7,8</sup> and integrated magnet-based logic circuits,<sup>9,10</sup> the electric-field control of magnetism can provide broader benefits to other research communities, like nanobiotechnology,

nanomedicine, and nanobiophysics,<sup>11,12</sup> that incorporate magnetic nanoparticles with a focus on device applications. For example, microfluidic laboratory setups require bulky table-top external magnets to manipulate medically and biologically functionalized superparamagnetic microbeads,<sup>13–16</sup> magnetic nanoparticles,<sup>17</sup> and biologically inspired magnetic swimmers.<sup>18,19</sup> Unfortunately, these magnetic-field-controlled schemes are impractical and energy-inefficient on the small scale. Replacing these methods with an electric-field-based control of magnetism<sup>1–5</sup> using multiferroic<sup>20</sup> heterostructures provides an ultra-low-power pathway to achieve similar degrees of mechanical control in a scalable on-chip platform. Initial efforts have verified electric-field-driven, strain-based magnetic

\* Address correspondence to [rcandler@ee.ucla.edu](mailto:rcandler@ee.ucla.edu).

Received for review October 2, 2014 and accepted April 23, 2015.

Published online April 23, 2015  
10.1021/nn5056332

© 2015 American Chemical Society

DW generation and manipulation in ferromagnet/piezoelectric heterostructures with magnetically patterned wires<sup>9</sup> and rings,<sup>21</sup> respectively, but deterministic manipulation of the DW position has yet to be demonstrated. Because of this limitation, little effort has focused on the electric-field control of external systems (e.g., magnetic particles) in fluidic environments. In this work, we experimentally demonstrate deterministic electrically driven, strain-mediated domain wall (DW) rotation in ferromagnetic Ni rings fabricated on piezoelectric  $[\text{Pb}(\text{Mg}_{1/3}\text{Nb}_{2/3})\text{O}_3]_{0.66}-[\text{PbTiO}_3]_{0.34}$  (PMN–PT) substrates. These results are confirmed with analytical predictions from a coupled micromagnetic/elastic model. Using this electric-field-based multiferroic control scheme, we experimentally control the position of suspended magnetic particles magnetostatically attracted to the Ni ring DWs on the PMN–PT surface with micrometer-scale precision.

Manipulating meso- and nanoscale objects in biology, chemistry, physics, medicine, and nanolithography is an important scientific and engineering challenge. Established techniques such as optical tweezers,<sup>22,23</sup> electrical tweezers,<sup>24</sup> and surface acoustic waves (SAW)<sup>25</sup> are used to capture, manipulate, and transport a variety of elements such as nanoparticles,<sup>23,24,26</sup> nanowires,<sup>24</sup> microbeads,<sup>27</sup> DNA,<sup>28</sup> and bacteria.<sup>29,30</sup> An optical tweezer setup, using laser-based trapping, provides a large degree of control but also requires a dedicated optical setup. These large setups are unsuitable for scalable lab-on-a-chip applications. Alternatively, both electrical tweezers<sup>24</sup> and SAWs<sup>25</sup> use on-chip electric fields to transport suspended particle ensembles. However, electric tweezers are limited to applications involving metallic nanowires, whereas the focus of SAW devices is on long-range transport rather than the local manipulation of an individual particle. Recently, a magnet-based technique was demonstrated,<sup>13,14</sup> exploiting the magnetostatic coupling between superparamagnetic microbeads (SPMs) and localized stray magnetic fields emitted from magnetic DWs in lithographically patterned micrometer-sized permalloy rings. The permalloy rings are initially magnetized into an “onion” state, with two parallel circumferential domains aligned along the magnetic field axis separated by two DWs.<sup>31</sup> The DWs produce localized stray magnetic fields that attract SPMs to the precise DW location along each ring, trapping them within a local magnetostatic potential. An external electromagnet drives the DWs around the circumference of each ring, and the magnetostatically coupled SPMs follow this DW motion. Although interesting, this approach requires bulky, high power electromagnets to create the external magnetic fields that control the DW positions. As stated previously, this approach restricts both the energy efficiency and practical device scaling. In contrast to this method,

we demonstrate a particle manipulation technique that uses scalable low-profile electrodes on composite multiferroic heterostructures to generate low-power, electric-field-induced strains that drive the rotation of the SPM–DW magnetostatic potential well along the ring circumference.

In this work, we first create stable magnetic onion states in lithographically patterned Ni rings fabricated on a piezoelectric PMN–PT substrate. These onion states contain DWs that are then deterministically rotated approximately  $45^\circ$  by an electric-field-induced strain that modifies the magnetic energy state of the Ni rings via inverse magnetostriction (i.e., Villari effect).<sup>21,32</sup> A  $0.8 \text{ MV m}^{-1}$  out-of-plane electric field produces in-plane anisotropic strains of 4000 ppm that move the DWs. We experimentally characterize the onion state formation and DW rotation with X-ray magnetic circular dichroism photoemission electron microscopy (XMCD-PEEM)<sup>33,34</sup> at the Advanced Light Source at Lawrence Berkeley National Laboratory. The magnetostrictive mechanism that drives the DW rotation behavior is confirmed with a multiphysics model<sup>35</sup> that fully couples Landau–Lifshitz–Gilbert (LLG) micromagnetics with elastodynamics to predict the DW formation and motion as a function of applied electric fields. Once DW motion is demonstrated, we magnetostatically couple commercially available, biologically and medically functionalizable suspended SPMs (Dynabeads from Life Technologies, Grand Island, NY, USA) to the onion state DWs of the nanoscale Ni rings. An electric field induces a strain that rotates the DWs and attached SPMs; this is in sharp contrast to previous demonstrations<sup>13–17</sup> that required external magnetic fields. The SPM motion is observed with conventional optical microscopy, and the SPM–DW coupling forces are estimated using micromagnetic simulations.

## RESULTS AND DISCUSSION

**Characterizing the Domain Wall Initialization.** To reliably obtain onion state DWs, we first characterize and model the DW formation as a function of ring geometry both experimentally and with conventional micromagnetic OOMMF simulations.<sup>36</sup> Using electron-beam lithography, we fabricate a number of ferromagnetic Ni rings (15 to 45 nm thick) with outer diameters (OD) ranging from 1 to  $2 \mu\text{m}$  while systematically varying the ring widths ( $W$ ) from 650 to 150 nm (Figure 1a, inset) on the surface of a Pt-coated (front and back)  $500 \mu\text{m}$  thick  $[\text{Pb}(\text{Mg}_{1/3}\text{Nb}_{2/3})\text{O}_3]_{0.66}-[\text{PbTiO}_3]_{0.34}$  substrate. The Pt acts as an electrode for the PMN–PT substrate. XMCD-PEEM<sup>33,34</sup> (Figure 1b, Methods) is used to obtain magnetic contrast images of our multiferroic heterostructures (Figure 1a).

Prior to PEEM imaging, each magnetic ring sample is initialized with a 3 kOe external magnetic field to create an onion state. The stability of the onion state

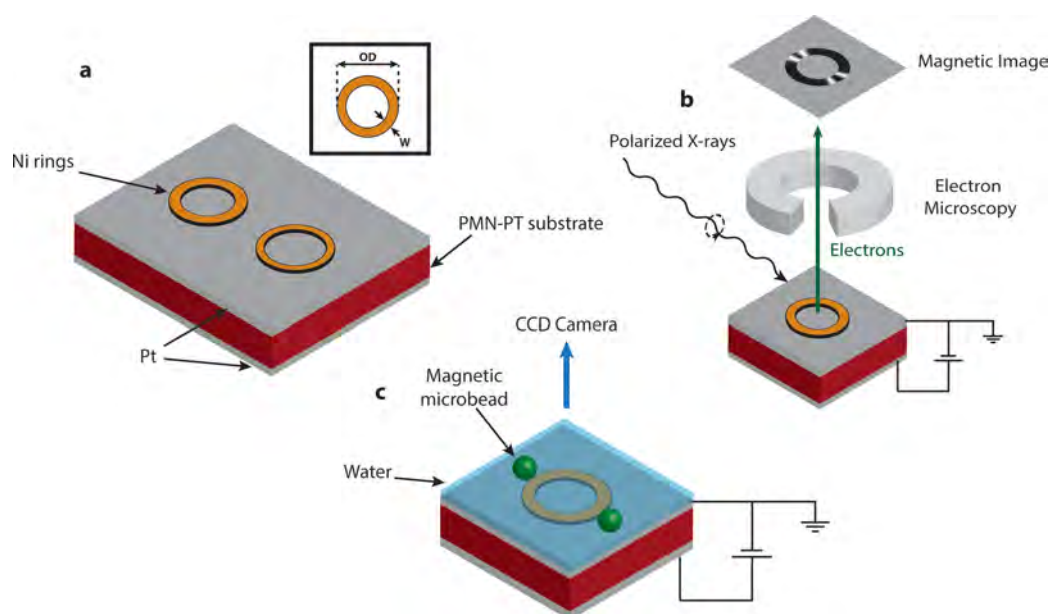


**Figure 1.** Sample design and experimental interrogation methods. (a) Schematic of a composite multiferroic heterostructure consisting of ferromagnetic Ni rings fabricated on the Pt-coated surface of a PMN–PT substrate. The backside of the PMN–PT substrate is also Pt-coated. Inset: Relevant outer diameter (OD) and width ( $W$ ) ring dimensions. (b) Magnetic properties of the Ni rings are observed by XMCD-PEEM with an *in situ* out-of-plane electric field applied across the substrate as indicated. (c) Position of SPMs, suspended in water, coupled to the on-ion-state stray fields is observed by conventional microscopy as a function of the out-of-plane substrate electric field.

upon removal of the initialization field depends on the ring dimensions.<sup>37</sup> OOMMF micromagnetic simulations<sup>36</sup> (Methods) were used to calculate the minimized magnetic energy density as a function of the  $W/OD$  ratio after initialization in 30 nm thick rings with an OD of 1, 1.5, 2, and 4  $\mu\text{m}$  (Figure 2a) and in 15 nm thick rings with an OD of 1 and 2  $\mu\text{m}$  (Figure 2b). For the 30 nm thick rings (Figure 2a), we observe three distinct energy density minima regimes with decreasing  $W/OD$  for each OD value: (1) the vortex state (i.e., where the ring magnetization is circularly oriented along the circumference with no DWs), in the bottom right corner (shaded in green), representing the lowest total energy density on the plot, (2) the onion state, in the middle of the figure (not shaded) that contains vortex-like DWs, and (3) the onion state, in the upper left of the figure (shaded in blue) that contains transverselike DWs and has the largest total energy density.

Figure 2c–e shows XMCD-PEEM images, whereas Figure 2f–h shows simulated micromagnetic images for 30 nm thick, 2  $\mu\text{m}$  OD rings with widths varying from 200 to 650 nm following initialization (as indicated in Figure 2a). The exchange (favoring parallel domains and local alignment of the magnetization) and demagnetization (favoring closure domains and minimization of the stray magnetic fields) energies are the dominant contributions to the total energy shown in Figure 2a, and these compete to rearrange the micromagnetic magnetization properties of the Ni rings into the lowest accessible energy state as indicated by the three regions of Figure 2a. In the initialized state, there is a high local energy density associated

with the ends of the onion state where the magnetization vector fields point toward a ring wall (a large demagnetization component). The redistribution of this high local energy density, upon removal of the external 3 kOe magnetic field, is dependent upon the  $W/OD$  parameters of the ring. The gradient of the local energy density relative to the energy density of a slightly perturbed magnetization configuration represents the driving force on the magnetization causing it to move to a stable or metastable state (i.e., if a magnetization configuration slightly different than the current state has lower energy, then the system experiences a force pushing it toward the new state). The large initial demagnetization energy in wider rings dominates the exchange energy component, driving the ring into the vortex state (Figure 2e and h and bottom right of Figure 2a). This vortex state forms because the demagnetization energy required to rotate the magnetization  $180^\circ$  for a wide ring is relatively low compared to the exchange energy. The high local energy density of the initialized state can overcome the local exchange energy barrier, and the magnetization along one-half of the ring flips direction, producing a vortex ring state.

As the ring width narrows, the demagnetization energy required to rotate the magnetization  $180^\circ$  becomes higher. This causes the perturbation states associated with rotating the magnetization past a wall to be relatively high. As the ring width narrows such that  $W/OD \approx 0.3$ , the driving force supplied by the demagnetization energy to rotate the magnetization no longer overcomes the exchange energy and

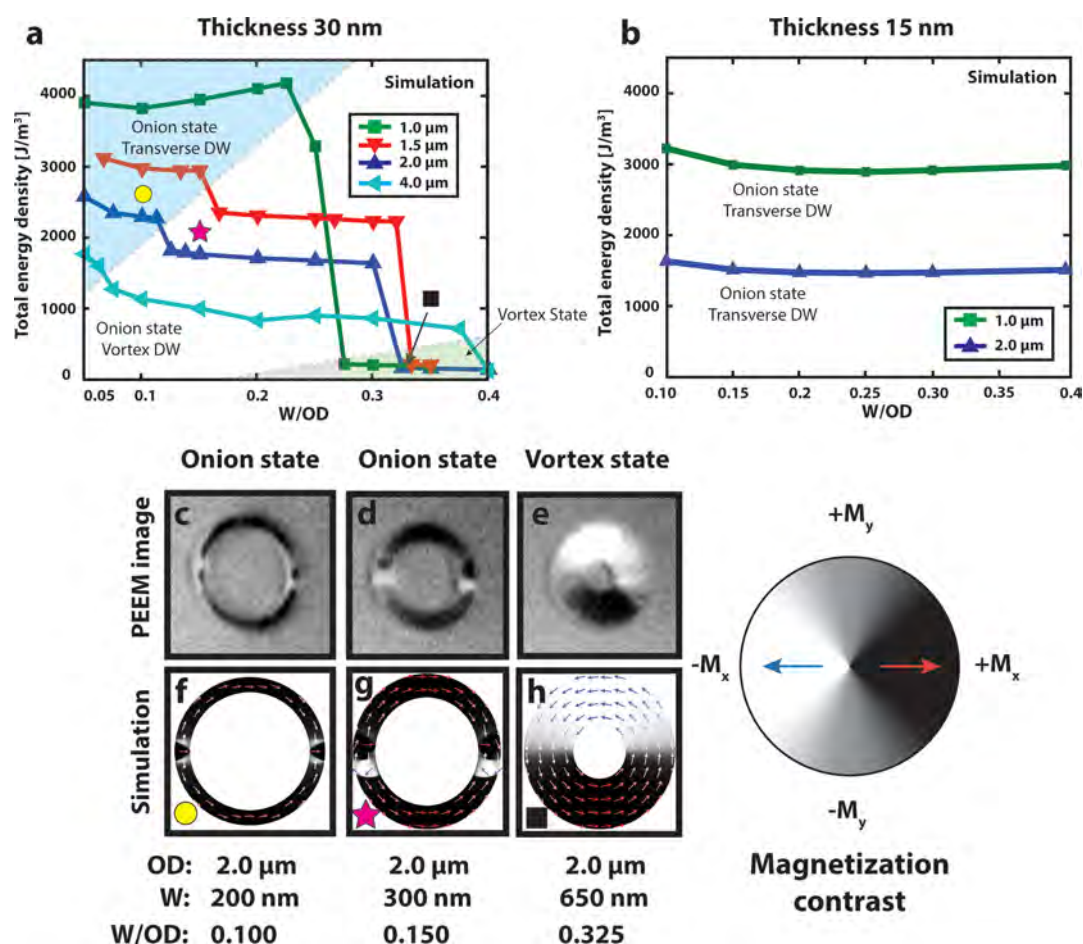
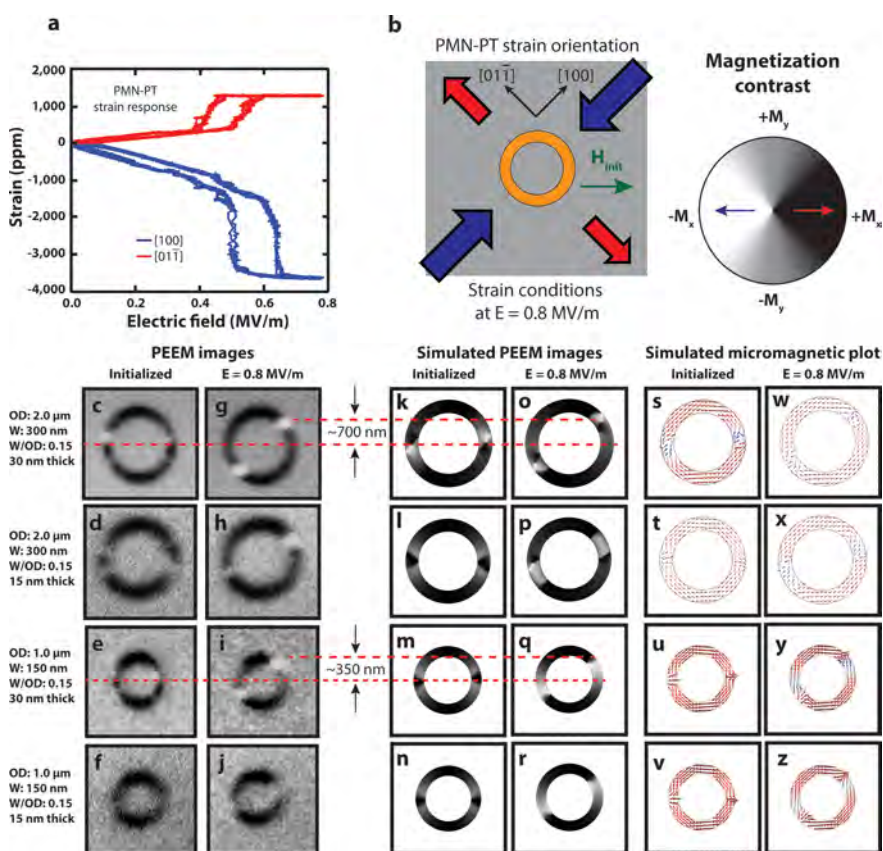


Figure 2. Initializing a stable onion state. Total energy density (assuming room temperature constants) calculated from micromagnetic simulations of (a) 30 nm thick, 1, 1.5, 2, and 4  $\mu\text{m}$  OD rings and (b) 15 nm thick, 1 and 2  $\mu\text{m}$  OD rings as a function of  $W/OD$  after the application and removal of a 3 kOe field in the absence of a thermal environment. In a, the three distinct regions (highlighted in green, white, and blue) correspond to the three possible initialized magnetization states: a vortex state, an onion state with vortex DWs, and an onion state with transverse DWs. Dashed lines are a guide to the eye. (c–e) XMCD-PEEM images taken at room temperature of 30 nm thick, 2  $\mu\text{m}$  OD rings with widths of 200, 300, and 650 nm, respectively. (f–h) Complementary micromagnetic simulations for rings with geometries identical to those in parts c–e. Black and white contrast orientation is identical to PEEM images, and the red and blue colored arrows indicate the magnetic orientation of individual grid elements from the micromagnetic simulation. The yellow circle, pink star, and black square indicate where each simulated geometry (and  $W/OD$  ratio) is located on the graph in part a.

extrinsic domain wall pinning because of edge roughness, leaving the ring in an onion state once the field is removed (Figure 2c,d,f,g). The high energy density tends to redistribute into a local vortex domain wall. As the  $W/OD$  ratio decreases further, the gradients between neighboring states continue to decrease, and the onion state itself becomes metastable (i.e., two possible DW types: vortex and transverse). Although these simulations show a transition between the DW type (vortex to transverse DW) as a function of the ring geometry, they do not account for thermal effects that can influence the nature of the DWs at room temperature.<sup>38</sup> Coupled with the fact that the PEEM resolution limits our ability to identify the precise type of DWs we obtain in thinner rings that are 30 nm thick, this means we cannot conclusively state where the precise vortex to transverse DW transition occurs. Nevertheless, the simulations shown in Figure 2a are in qualitative agreement with our PEEM imaging

measurements, and the results confirm that stable onion states are achievable in 30 nm thick Ni rings with  $W/OD \leq 0.3$ , as identified by the model in Figure 2a.

The OOMMF simulations<sup>36</sup> of the 15 nm thick rings (Figure 2b) do not show a  $W/OD$  dependence between onion states and vortex states in either the 1 or 2  $\mu\text{m}$  OD rings up to  $W/OD = 0.4$ . Instead, in all cases, an onion state with transverse DW is observed. These thinner rings are exchange-dominated and do not possess the requisite demagnetization energy required to flip the magnetization direction radially past a ring wall. From Figure 2a,b, we find that the properties of the onion state DWs are dependent on the ring thickness,<sup>39</sup> with thinner rings having a higher probability to form transverse DWs (Figure 4c,f). Although our OOMMF model confirms a previous study<sup>14</sup> that found transverse DWs produce stray magnetic fields with larger magnitudes as indicated by the higher energy densities, for the application of trapping



**Figure 3.** Electrically driven submicron domain wall rotation. (a) A typical strain response along the  $[100]$  and  $[01\bar{1}]$  directions of a PMN–PT substrate as a function of an out-of-plane electric field. (b) Schematic illustrating the initialization field ( $H_{\text{init}}$ ) direction with respect to the PMN–PT  $[100]$  and  $[01\bar{1}]$  directions and the compressive and tensile strain response along each direction at  $0.8 \text{ MV m}^{-1}$ . (c–j) XMCD-PEEM images showing the initialized (c–f) and electrically rotated (g–j) onion states in 30 and 15 nm thick rings with  $\text{OD} = 2 \mu\text{m}$ ,  $W = 300 \text{ nm}$  and  $\text{OD} = 1 \mu\text{m}$ ,  $W = 150 \text{ nm}$ . (k–r) Simulated images from the coupled micromagnetic/elastic model of initialized (k–n) and electrically rotated (o–r) rings with dimensions identical to the rings in parts c–j. The color scale contrast of the simulated micromagnetic orientation is scaled to match the contrast obtained with XMCD-PEEM. (s–z) Micromagnetic plots from the same simulations shown in parts k–r showing the orientation of individual grid elements from the model. Red and blue arrows indicate the relative orientation direction. Dashed red lines are eye guides and indicate the DW displacement for each ring after strain is applied.

magnetic microbeads, the distinction between the two DW types is not critical.

**Electric Field Control of Domain Wall Rotation.** Selecting 30 and 15 nm thick Ni rings with  $W/\text{OD} < 0.3$ , we experimentally demonstrate deterministic DW rotation by applying an electric field to the PMN–PT substrate. The rhombohedral single-crystal PMN–PT used in this study has a spontaneous polarization along the  $\langle 111 \rangle$  direction, and the  $\langle 011 \rangle$  cut of these substrates give large in-plane anisotropic strains upon the application of an electric field across the substrate.<sup>40</sup> On the basis of previous work,<sup>21,41,42</sup> the electric-field-induced strain in the piezoelectric substrate modifies the magnetoelastic energy component ( $H_{\text{me}}$ ) of the Ni to create energetically favorable conditions that can reorient the DWs toward the dominant compressive strain axis (Methods). Figure 3a shows the electric-field-induced strain in the poled PMN–PT sample characterized with a strain gauge along the in-plane  $[100]$  and  $[01\bar{1}]$  directions. A  $0.8 \text{ MV m}^{-1}$  electric field produces a 4000 ppm differential uniaxial compressive strain in

the  $[100]$  direction and a 1300 ppm differential tensile strain in the  $[01\bar{1}]$  direction (Figure 3b). The hysteretic strain jump at  $E \approx 0.5 \text{ MV m}^{-1}$  is a result of a morphotropic phase transition in the PMN–PT<sup>43</sup> sample, but upon removal of the electric field, the strain returns to zero. The applied anisotropic strain state should produce a rotation of the DWs toward the  $[100]$  direction<sup>21</sup> because of the fact that Ni is a negative magnetostrictive material. In the following analysis and discussion, we assume the as-deposited Ni structures are initially unstrained.

Figure 3c–f shows the XMCD-PEEM images of initialized onion states in a  $2 \mu\text{m}$  OD, 300 nm wide and  $1 \mu\text{m}$  OD, 150 nm wide ring for both 30 nm (Figure 3c,e) and 15 nm (Figure 3d,f) thicknesses, respectively. Plotted next to the PEEM images in Figure 3 are simulated PEEM images of rings with identical geometries (Figure 3k–n) and their corresponding micromagnetic plots (Figure 3s–v) calculated from a micromagnetic/elastic model<sup>35</sup> performed in COMSOL Multiphysics that directly solves

the coupled micromagnetic, piezoelectric, and elastodynamic partial differential equations to determine the magnetization dynamics of the Ni ring geometries with respect to the electrical response of the piezoelectric substrate (Methods). A 3 kOe external magnetic field is applied to each sample and simulation at a 45° angle relative to the [100] strain axis, as indicated in Figure 3b, to initialize an onion state. We note that the resulting onion-state vortex DWs have an equal probability of being clockwise- or counterclockwise-oriented (compare Figure 3c,k); however, this DW helicity does not impact the magnetic response because of strain. In the XMCD-PEEM study, an image of the magnetic state of the rings is recorded at 0.04 MV m<sup>-1</sup> intervals up to a maximum electric field of 0.8 MV m<sup>-1</sup>. Supporting Information Video 1 is a series of XMCD-PEEM images taken of the 2 μm OD, 300 nm wide, 30 nm thick ring during this process. Near the critical electric field where the large strain jump occurs in Figure 3a, we observe a piecewise DW reorientation along the compressive [100] strain axis of the PMN–PT substrate, indicated in Figure 3g–j for each ring, as compared to their initial states, shown in Figure 3c–f, respectively. This electrically generated piecewise DW rotation is also predicted in the simulated PEEM images and their corresponding micromagnetic plots in Figure 3o–r and Figure 3w–z, respectively. The electrically driven, strain-mediated DW rotation in the simulated Ni rings agrees well with our experimental observations.

For both the simulations and experiment, no further DW response is observed at higher electric fields. The strain applied in the PEEM images is global and affects all the patterned structures on the surface. This is evident in Supporting Information Video 2, which is a zoomed out view of the same ramping process shown in the first video. The video includes many rings and disks of multiple sizes that show similar DW rotation. The behavior we see demonstrates a deterministic manipulation of the DW defined by the relative orientation of the initialized magnetization direction and PMN–PT strain axis. However, similar experiments where the DWs were initialized 90° relative to the PMN–PT [100] axis showed little DW rotation response. In this case, clockwise and counterclockwise DW rotations are equally probable, and experimental results for this initialization scenario have shown both a low tendency to rotate and an approximately equal clockwise and counterclockwise rotation in rings where significant rotation is observed. Furthermore, micromagnetic/elastodynamic simulations of this case in a 30 nm thick, 2 μm OD, 300 nm wide ring reveals no significant rotation of the initialized DWs with a strain of up to 10 000 ppm applied (more than twice the amount of strain we are experimentally capable of applying). Instead, new DWs are formed along the PMN–PT [100] axis, 90° offset from the existing

initialized DWs when a strain of 5000 ppm is applied. In general, we have found it is experimentally challenging to rotate the domains walls from a 90° offset.

With the magnetic response to an applied electric-field-induced strain measured, we now investigate the magnetic response as a function of Ni thickness and electric field cycling. Ramping the electric field down to 0 MV m<sup>-1</sup> produces different final magnetic states depending on the ring thickness, which can be explained in terms of induced strain. All the rings are subject to shear lag effects,<sup>44,45</sup> where strain varies through a structure as a function of position from a free edge. This shear lag effect is well-known in the mechanics community studying finite-size structures. The effects of this shear lag are explicitly shown in the Supporting Information, section S1, where we plot the volumetric strain profile, as calculated by the COMSOL model, of a cross section across the ring width for 15, 30, and 45 nm thick rings with identical dimensions. These shear lag effects attenuate the influence of the magnetoelastic coupling as a function of ring thickness. It is also important to point out that XMCD-PEEM is a surface-sensitive technique that measures the magnetic orientation of only the top few nanometers in the rings.<sup>46</sup> In Figure 4a–n, PEEM images are shown for a 2 μm OD, 300 nm wide ring of each thickness (15, 30, and 45 nm) at different applied electric fields. The DWs in the 45 nm thick ring (Figure 4a,b) do not exhibit large movements in response to the electric-field-induced strain. Upon applying the electric field, the relatively thicker ring has a large shear lag dependence, producing more inhomogeneous strains that reduce the effective strain present at the Ni surface; thus, we do not observe significant DW motion. Both the presence of an inhomogeneous strain state and the inability to electrically move DWs in 45 nm thick rings has been confirmed with the micromagnetic/elastodynamic model (Supporting Information, section S1).

As the thickness of the ring is reduced from 45 to 30 nm, the DW movement response to the electrically driven strain becomes more significant (Figure 4c–f). This DW movement in the 30 nm ring is directly related to both the larger effective surface strain (reduced shear lag) as well as the presence of a more homogeneous strain state through the thickness (Supporting Information, section S1). As can be seen in Figure 4d, the DW was successfully rotated by 45° toward the PMN–PT [100] axis. Applying strain in this case introduces a tunable source of magnetoelastic energy that competes with the existing shape anisotropy and exchange energies of the initialized rings to reorient the magnet. As tensile strain, along the [01 $\bar{1}$ ] axis, and compressive strain, along the [100] axis, increase, an easy axis is created along the [100] axis because of the inverse magnetostriction effect. This increases the magnitude of the magnetoelastic energy, which is proportional to

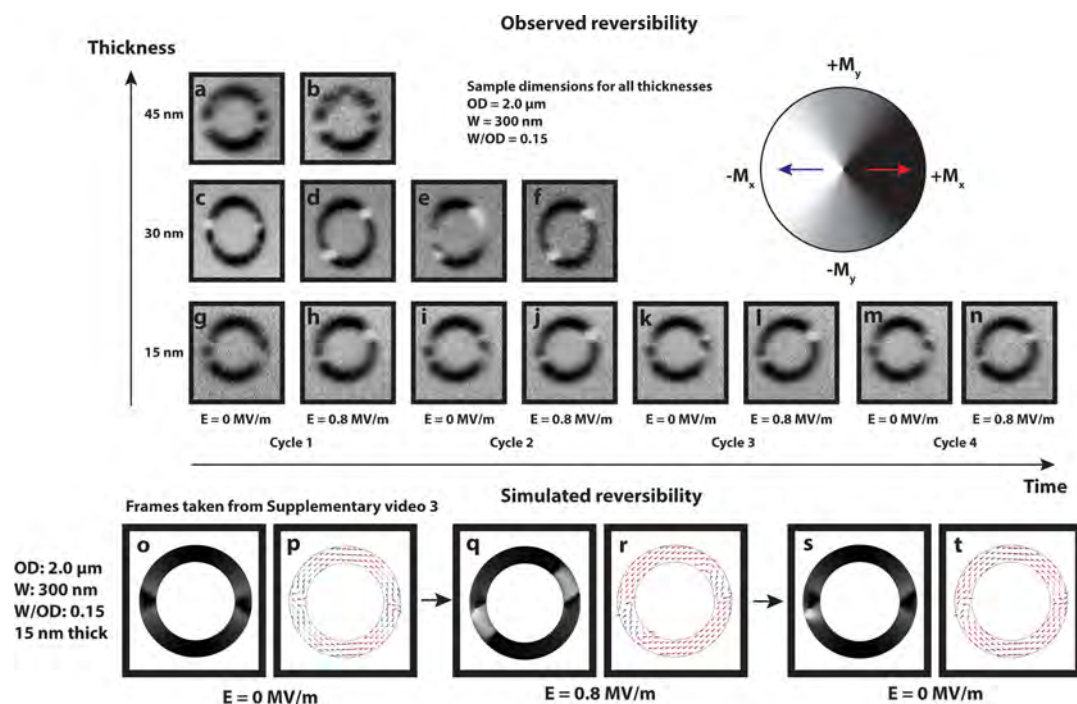


**Figure 4.** Thickness-dependent cycling behavior. Surface magnetic state for rings with identical lateral dimensions ( $2\ \mu\text{m}$  OD,  $300\ \text{nm}$  width) but with varying thicknesses  $45\ \text{nm}$  (a and b);  $30\ \text{nm}$  (c–f); and  $15\ \text{nm}$  (g–n) plotted as a function of electric field cycling. (a and b) The  $45\ \text{nm}$  thick ring displays little to no DW rotation behavior upon the initial cycle. (c–f) For  $30\ \text{nm}$  thick rings, we observe a DW rotation after the first cycle; however, the rotated domain broadens back toward its initial state as the electric field is removed. This is due to magnetic relaxation, possibly driven by local remanent strains, in the rings as the strain is removed. Cycling the  $30\ \text{nm}$  thick ring a second time reproduces the rotated DW state. (g–n) The  $15\ \text{nm}$  thick sample displays reproducible elastic DW rotation behavior over 4 cycles as a function of the applied electric field. (o–t) Simulated images (o, q, and s) and micromagnetic plots (p, r, and t) from the coupled micromagnetic/elastic model video shown in Supporting Information Video 3. Parts o and p show an initialized  $15\ \text{nm}$  thick,  $2\ \mu\text{m}$  OD, and  $300\ \text{nm}$  width ring. Parts q and r demonstrate magnetic domain wall motion and broadening as a result of a simulated electric field of  $0.8\ \text{MV m}^{-1}$ . Parts s and t illustrate that the magnetization returns to a state similar to the initialized state shown in parts o and p after the simulated electric field is removed.

$\cos^2 \theta$ , where  $\theta$  is the angle between the magnetization and the compressive strain direction, making the Ni structures more energetically favorable to rotate toward the  $[100]$  axis (Supporting Information, section S2). This occurs as long as the change in the total magnetic energy caused by the magnetoelastic energy outweighs any significant changes to the exchange or demagnetization energies present during reorientation. As shown in Figure 3 and Figure 4c,d for  $30\ \text{nm}$  thick rings and Figure 4g,h for  $15\ \text{nm}$  thick rings, when a strain is transferred more uniformly through the thickness of the ring, the onion states are more likely to rotate toward the new magnetic energy minimum generated along the PMN–PT  $[100]$  axis.

In Figure 4e and Supporting Information Videos 1 and 2, we observe magnetic domains broadening when the electric field is removed instead of remaining stationary. This broadening suggests that an elastic force is present that drives a portion of the domain back toward its initial position. As previously stated, we have assumed the Ni rings are initially unstrained and removal of the electric field should not provide such a driving force. As shown in Figure 3a, we expect that reducing the electric field returns the sample to

a zero-strain state, thus removing the contribution of magnetoelastic energy to the overall magnetic energy. Assuming the exchange and shape anisotropies remain constant and the absence of remanent strain, reducing the magnetoelastic energy should not alter the magnetic DW orientation stabilized along the new energy minimum. Thus, this observation of domain broadening suggests that a re-evaluation of the zero-initial-strain assumption is required.

It is important to note that the influence of the electric-field-induced strain on the magnetization of the fabricated structures critically depends on the initial value of the strain imposed on the Ni structures at the time of deposition.<sup>42</sup> Although the samples were prepoled prior to the Ni deposition step,<sup>40</sup> the Ni rings still remain subject to local strain variations because of the presence of micrometer-scale ferroelectric domains in the PMN–PT, which we have observed with piezo-response force microscopy (Supporting Information, section S3).<sup>42</sup> It is reasonable to assume that the  $1$  and  $2\ \mu\text{m}$  OD Ni rings from our samples span multiple PMN–PT ferroelectric domains that may be oriented along the two out-of-plane  $\langle 111 \rangle$  polarization directions and along the four in-plane  $\langle 111 \rangle$  polarization directions.

A reorientation of these domains along different vectors after deposition and fabrication of the Ni rings (e.g., caused by the application of electric field) generates a localized remanent strain that has been previously reported.<sup>40,42</sup> Although we believe it is unlikely, another source of remanent strain may be attributed to our fabrication process. After prepoling the PMN–PT substrates, Ni films were electron-beam-evaporated onto these substrates at a process temperature of approximately 50 °C. This temperature might have partially depoled the substrate (i.e., reoriented the surface  $\langle 111 \rangle$  polarizations), resulting in a small remanent strain.<sup>47</sup>

Re-evaluating our system leads to the following assertion. Stable onion states are formed through the energy minimization process involving the demagnetization and exchange energies in the presence of localized remanent strains which may contribute a small magnetoelastic energy to the total energy. Applying an electric field makes the magnetoelastic energy dominant and drives the onion state toward a new orientation that is based along the dominant PMN–PT strain axis, as discussed before. However, when the electric field decreases, rather than return to a net-zero-strain state, the dominant magnetoelastic energy provides a back-driving force that serves to relax the local magnetization toward its initial remanent state. Thus, the final magnetic state observed in the 30 nm thick rings (Figure 4e) consists of a domain broadened between the strain-generated easy axis along the PMN–PT [100] direction and the initialized magnetic direction that is 45° from the [100] direction.

The 15 nm thick rings are subject to similar local strain cycling conditions; however in this case, the relatively thinner layer (compared to the 30 nm thick rings) reduces the magnetic relaxation degrees of freedom by favoring a more dominant exchange contribution to the total magnetic energy at the expense of both the demagnetization energy and the electrically generated magnetoelastic energy contributions.<sup>39</sup> The strain-induced magnetoelastic energy does not dominate the total magnetic energy for these rings; instead, it perturbs the magnetic domain to rotate slightly toward the [100] axis (Figure 4h) at 0.8 MV m<sup>-1</sup>. Removing the electric field appears to return the magnetic domain back to its original position (Figure 4i). It is most likely driven back to its original state by the additional magnetic stiffness imposed by the exchange and demagnetization conditions for this thickness as well as any unintentional remanent strain contributions. Cycling the electric field in the 15 nm thick ring case (Figure 4g–n) confirms the repeatability of this apparent elastic DW behavior. Additional magnetic images in Supporting Information, section S4 of an energetically unconstrained 2 μm, 30 nm thick Ni disk (fabricated on the same sample as the rings) provides further evidence for the presence of a localized remanent strain which tends to drive a cyclical

reorientation of a magnetic domain in the disk by 90° as a function of the applied electric field.

The elastic DW broadening we observe in Figure 4e in the 30 nm thick ring and the cyclical DW reorientation we observe in Figure 4g–n in the 15 nm thick ring are a result of the total magnetic energy rebalancing after the strain is tuned through multiple cycles. This magnetic energy minimization process, induced by tuning the magnetoelastic energy, forms the basis of the coupled micromagnetic/elastic model used to verify the PEEM results in Figure 3. We note that these simulations assume no initial strain and do not account for the remanent strain and ferroelectric domains we experimentally observed. The majority of our simulations did not exhibit the elastic relaxation behavior we observe with PEEM; instead, the magnetic domains remained fixed in their new positions. This is why we have attributed the observed relaxation behavior to remanent strain. However, one simulation of a 15 nm thick, 2 μm OD, 300 nm wide ring (Figure 4o–t and Supporting Information Video 3) produced an elastic behavior despite the lack of initial and remanent strain built into the model. It serves as an example to demonstrate the magnetically stiff conditions in the 15 nm thick samples created by the higher exchange energy contribution, which can contribute to the elastic behavior of the domain wall as a function of electric field cycling. After initializing the onion state (Figure 4o,p), the additional magnetoelastic energy produced by a simulated electric field of 0.8 MV m<sup>-1</sup> creates an easy axis (and energy minimum) 45° relative to the magnetic initialization axis and along the [100] direction (Figure 4q,r). A domain forms in the simulation with DWs at both the new energy minimum along the [100] direction and along the initialized direction. Removing the simulated electric field decreases the magnitude of the magnetoelastic energy in the system, and the relative exchange and demagnetization energies drive the domain to elastically return to its original configuration (Figure 4s,t). We observe a relaxation of the magnetization back to an energy condition similar to (but not identical with) the initialized state.

From this analysis, we conclude that the 45 nm thick rings, for the diameters studied, are too thick to adequately transfer the strain to alter the magnetic energy landscape (i.e., shear lag effect). The initialized DWs in 30 nm thick rings, for the ring diameters studied, are sensitive to the electrically driven strain, but their relatively large thickness creates a less-constricted magnetic environment that leaves these rings susceptible to local environmentally generated strains. Finally, magnetic domains in the 15 nm thick rings, for the ring diameters studied, also show electrically driven DW behavior, but in this case, the constricted magnetic environment leads to an elasticlike domain reorientation upon cycling. We also note that

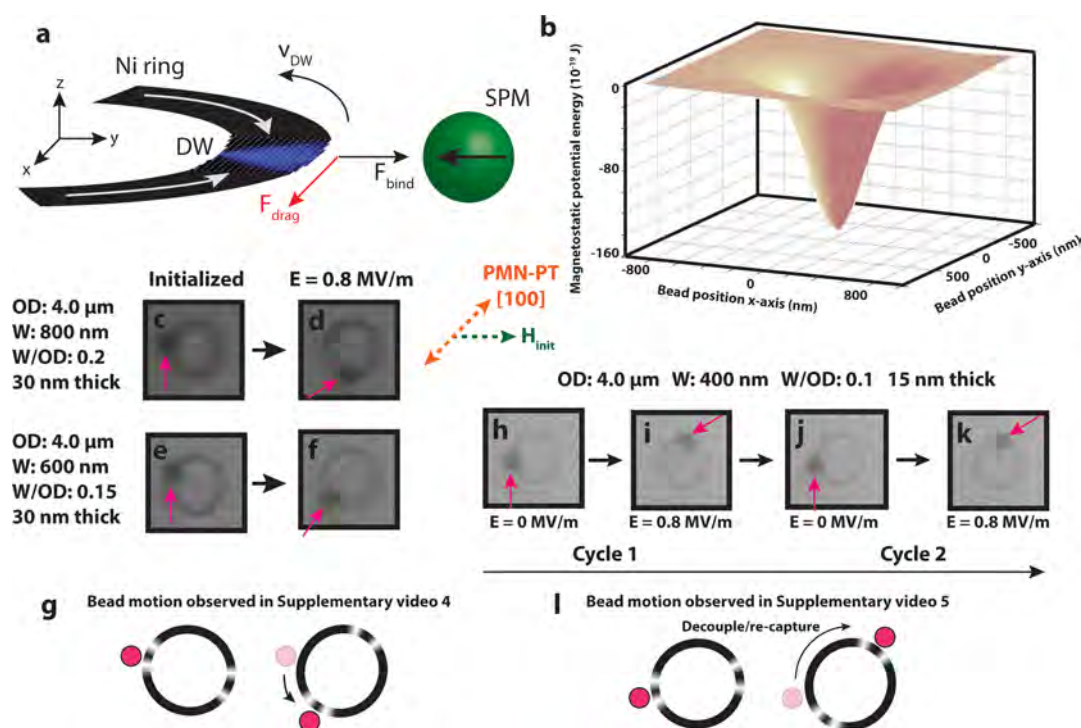


**Figure 5.** Electrically driven displacement of magnetically trapped SPMs. (a) Schematic, containing an OOMMF simulation of a Ni ring DW, illustrating the attraction force ( $F_{\text{bind}}$ ) between the SPM and DW and the DW velocity ( $v_{\text{DW}}$ )-dependent viscous drag force ( $F_{\text{drag}}$ ). (b) The magnetostatic potential interaction between a 1  $\mu\text{m}$  diameter SPM and a DW in a 250 nm wide, 15 nm thick Ni ring as a function of the SPM lateral position with respect to the DW. (c–f) Contrast-enhanced still images taken from Supporting Information Video 4 showing the position of 1  $\mu\text{m}$  diameter SPMs (indicated by pink arrows) coupled to 4  $\mu\text{m}$  OD, 30 nm thick, 800 and 600 nm wide rings before (c, e) and after (d, f) applying a 0.8 MV  $\text{m}^{-1}$  electric field. (g) Conceptual explanation for the observed motion in Supporting Information Video 4; SPM tracks DW motion. (h–k) Contrast-enhanced still images taken from Supporting Information Video 5 showing the position of a 1  $\mu\text{m}$  diameter SPM (indicated by pink arrows) coupled to a 4  $\mu\text{m}$  OD, 15 nm thick, 400 nm wide Ni ring through two electric field cycles. (l) Conceptual explanation for the observed motion in Supporting Information Video 5; SPM decouples and is recaptured by a different DW on the same ring.

on the basis of the initial orientation of the DWs with respect to the PMN–PT [100] direction we can choose to deterministically rotate the DWs clockwise or counterclockwise. Though we only show data for one helicity, experiments for both helicities were performed and showed identical but symmetric behavior. Finally, as a metric for potential lab-on-a-chip applications, we note that the sample geometries used in this work are capable of producing piecewise, submicrometer DW displacements, 700 and 350 nm in the 2 and 1  $\mu\text{m}$  OD rings (Figure 3c,g and Figure 3e,i, respectively), without the assistance of an external magnetic field.

#### Characterizing the Electrically Driven Magnetic Bead Motion.

On the basis of the above results, we incorporate suspended SPMs (Methods) onto 30 and 15 nm thick rings (Supporting Information Videos 4 and 5, respectively) with  $W/\text{OD}$  ratios below 0.3. The position of SPMs attached to the rings is imaged using conventional optical microscopy as a function of the applied electric field (Figure 1c, Methods). The SPMs are initially attracted to the DW stray fields and become magnetostatically trapped in the DW potential well (Figure 5a,b)<sup>13,14</sup> by a binding force,  $F_{\text{bind}}$ . The magnitude of  $F_{\text{bind}}$  depends strongly on the ring thickness

and width (Supporting Information, section S5) and is directly related to the magnetic energy density calculated in Figure 2. Figure 5c,e shows still images captured from Supporting Information Video 4 of 1  $\mu\text{m}$  diameter SPMs coupled to DWs initialized in a 30 nm thick, 4  $\mu\text{m}$  OD, 800 and 600 nm wide ring, respectively. Figure 5d,f indicates the final position of each bead after the application of a 0.8 MV  $\text{m}^{-1}$  electric field.

As the electric field is applied, we observe the SPMs track the rotation of the DW toward the PMN–PT [100] axis; they abruptly move when the DW undergoes its piecewise motion (Figure 5g). As expected from the PEEM images, removing the electric field in the 30 nm thick rings does not reverse the positions of the SPMs. We repeat this process for a 15 nm thick, 400 nm wide ring in Figure 5h–k, which are still images taken from Supporting Information Video 5, but in this video, we ramp the applied electric field to values on both sides of the hysteretic strain jump over multiple successive cycles. An SPM couples to the thinner ring as before; however, during this ramping process we observe the SPM move piecewise across the ring beyond the expected 45° rotation and decouple completely from the ring (Figure 5l). This behavior is explained below.

In contrast to the 30 nm thick rings, the cyclical application of the electric field in the 15 nm thick rings creates and removes additional magnetic energy minima along the PMN–PT [100] axis, extending and retracting the DW and its associated stray fields. This results in the reproducible, pseudoreversible position control of the SPM beads attracted to the stray fields oriented along the PMN–PT [100] axis and agrees well with the behavior observed and discussed in Figure 4.

As observed in PEEM, the electric field drives piecewise DW realignment to the PMN–PT strain axis. The velocity of this DW motion,  $v_{\text{DW}}$ , plays a significant role<sup>13,14</sup> in maintaining the SPM–DW magnetostatic coupling within the fluidic environment. The binding force,  $F_{\text{bindr}}$ , in the fluid is opposed by a  $v_{\text{DW}}$ -dependent viscous drag force,  $F_{\text{dragr}}$ , opposite to the direction of motion<sup>48</sup> (Figure 5a and Supporting Information, section S5). At a critical  $v_{\text{DW}}$  near  $1 \text{ mm s}^{-1}$  for a  $1 \mu\text{m}$  diameter SPM,<sup>13</sup>  $F_{\text{drag}}$  overcomes  $F_{\text{bindr}}$ , and the bead decouples from its DW. From time-evolved simulations, we estimate an electrically driven DW velocity in the Ni rings on the order of  $50 \text{ m s}^{-1}$ . Because this is much greater than the critical  $v_{\text{DW}}$ , we observe many beads decouple from their initial DW positions during the application of an electric field then immediately recouple to stray fields in their new rotated positions. In Figure 5h–k, this gives the impression that the SPMs have rotated beyond  $45^\circ$ . A similar decoupling takes place in the 30 nm thick rings; however in this case, the SPMs are more strongly coupled to the ring (Supporting Information, section S5) and immediately recouple to the same DW in its new position. In the absence of magnetic contrast imaging, the SPMs act like markers that track the location of DWs and confirm that successful DW rotation has been achieved. However, the stray fields produced by the DWs remain experimentally uncharacterized and may vary from ring to ring, creating different SPM settling locations along each individual ring circumference (Figure 5d,f).

## METHODS

**Sample Preparation.** To minimize the generation of remanent strain in the Ni structures, Pt-coated  $[\text{Pb}(\text{Mg}_{1/3}\text{Nb}_{2/3})\text{O}_3]_{0.66}-[\text{PbTiO}_3]_{0.34}$  substrates are subjected to a  $0.4 \text{ MV m}^{-1}$  out-of-plane electric field prior to PEEM imaging to uniformly align the electric polarization throughout each sample. The Ni rings are evaporated on the Pt surface of the sample via an electron-beam lithography lift-off process.

**X-ray Magnetic Imaging.** The magnetic domain structure of our samples is characterized by photoemission electron microscopy (PEEM)<sup>33</sup> at beamline 11.0.1 of the Advanced Light Source (ALS) synchrotron at Lawrence Berkeley National Laboratory. Samples are placed in the high-vacuum PEEM chamber where circularly polarized X-ray light from the synchrotron ejects surface electrons, which are then accelerated by a sample bias of 18 kV into electron imaging optics (Figure 1b). We obtain magnetic contrast by X-ray magnetic circular dichroism (XMCD):<sup>34</sup> first tuning the X-rays to the Ni  $L_3$  absorption edge (853 eV), then exposing two images at the same location illuminated by right and left

Although not optimized, this control scheme introduces a pathway toward energy-efficient, all-electrical on-chip particle manipulation. Furthermore, as shown in Figure 3c,g and Figure 3e,i, the DW realignment is scalable to submicrometer-length scales in smaller ring structures; this may create opportunities to precisely position magnetic nanoparticles with nanoscale precision without the need for external magnetic fields.

## CONCLUSIONS

The  $v_{\text{DW}}$ -dependent coupling and DW positioning resolution of this proof-of-concept demonstration are currently limited by the initialization procedure and the global, out-of-plane electric field polarization, which restrict the present DW motion to a piecewise rotation. An alternative electric field geometry incorporating surface electrodes to generate localized strains may be more suitable to demonstrate smoother, electrically tunable rotation beyond  $45^\circ$ .<sup>49</sup> Additionally, future samples can be fabricated on PMN–PT substrates with less PT composition, such as  $\text{PMN}_{0.7}-\text{PT}_{0.3}$ , which possess a quasi-linear strain response ramping up to  $0.8 \text{ MV m}^{-1}$ , in contrast with the hysteretic strain response presented in Figure 3a, which is a result of an electric-field-induced phase transition.<sup>43</sup> Finally, we note that although this positioning technique is limited to magnetic particles, the surfaces of the commercially obtained SPMs used in this study can be customized with a variety of ligands including antibodies, proteins, and DNA and are used for a diverse set of biological and medical applications. With further refinement, this precision multiferroic positioning technology may be considered a viable candidate for incorporation with next-generation energy-efficient, compact lab-on-a-chip devices by providing a means to manipulate individual magnetic particles with only electric fields. This technology may also form the basis for electrically driven, strain-mediated nanoscale magnetic motors.

circularly polarized X-rays, respectively, and finally comparing these images by per-pixel numerical division. All measurements are performed at room temperature.

**Domain Wall–Magnetic Microbead Coupling Experiment.** Multiferroic stacks with 15 and 30 nm thick patterned Ni rings similar to those used in the PEEM experiment undergo the same initialization procedure and are then placed in an optical microscope. A drop of deionized water with suspended  $1 \mu\text{m}$  diameter SPMs is placed onto the composite multiferroic surface with a microscope coverslip (Figure 1c). We observe the position of the SPMs as we ramp the voltage across the PMN–PT substrate at  $0.04 \text{ MV m}^{-1}$  intervals. All measurements are taken in ambient conditions.

**Micromagnetic Simulations for Onion-State Initialization.** The object-oriented micromagnetic framework (OOMMF) eXtensible Solver is used to study the geometry-dependent formation of the onion state in the Ni rings<sup>36</sup> in Figure 2. OOMMF determines the final magnetization of an object by locally and globally solving the LLG equation at distinct locations along a 3D meshed

grid of the ring (thermal effects are ignored). The magnetization of each unit cell has three degrees of freedom. We choose the volume of a unit cell to be  $5 \text{ nm} \times 5 \text{ nm} \times 5 \text{ nm}$ , where each length is shorter than the exchange length of Ni,  $7.72 \text{ nm}$ . Additionally, the exchange stiffness constant,  $A$ , and the saturation magnetization,  $M_s$ , of Ni are assumed to be  $9 \times 10^{-12} \text{ J m}^{-1}$  and  $500 \text{ kA m}^{-1}$ , respectively. Simulating a  $3 \text{ kOe}$  magnetic field along one lateral axis saturates the magnetization in each unit cell of the ring. When the field is removed, the ring settles by an energy minimization process until the final relaxed state is achieved. We consider only exchange and demagnetization energies in the total magnetic energy and ignore the effect of magnetocrystalline energy. The magnetocrystalline anisotropy energy in polycrystalline Ni is relatively low compared to other terms.

**Modeling the Coupled Piezoelectric/Ferromagnetic Behavior.** We developed a numerical method on the basis of finite elements to fully couple micromagnetic simulations with elastodynamics (while ignoring thermal effects) in finite-size 3D structures<sup>35</sup> that we plot in Figure 3. The weak forms of micromagneto–electro–mechanical-coupled equations are solved using finite element methods with an implicit backward differentiation formula (BDF) time-stepping scheme. To decrease solution time, the system of equations with the dependent variables is solved using a segregated solution approach, which splits the solution process into substeps using a damped Newton's method. For all numerical problems, convergence studies (i.e., mesh size and time steps) were evaluated to ensure accuracy. The element size was chosen to be comparable to the exchange length, and the substrate and air were considered in the analysis. This coupled model provides an approach to simultaneously solve the full strain and micromagnetic spin distribution in the composite system as a function of position and time.

To adequately predict the magnetization states of the ferromagnetic ring structures as a function of electric field, it is necessary to model the magnetization dynamics using the LLG equation along with the mechanical stresses and strains via the equations of elastodynamics in the rings. For the substrate on which the rings are deposited, a piezoelectric model accounts for electric-field effects using a quasi-static electric field approximation and for displacement phenomena with the elastodynamics equations. The electrostatic assumption only eliminates coupling with magnetic field components and does not limit the applicability of this model to predict the dynamic response presented in this paper.

The theoretical framework for this problem reduces to seven coupled partial differential equations (PDEs) that solve for magnetization, displacement, and magnetic potential in the ferromagnetic rings and four coupled PDEs for the displacement and electric potential in the piezoelectric substrate. Modeling assumptions include small elastic deformations, linear elasticity, magnetostatics, electrostatics, and negligible electrical current contributions. The governing elastodynamic equations are

$$\rho \frac{\partial^2 \vec{u}}{\partial t^2} - \nabla \cdot \sigma = \vec{0} \quad (1)$$

where  $\rho$  is the density,  $\sigma$  is the stress tensor,  $\vec{u}$  is the displacement vector, and  $t$  is time. The LLG micromagnetic relation represents the second set of equations, expressed as

$$\frac{\partial \vec{M}}{\partial t} = -\mu_0 \gamma \vec{M} \times \vec{H}_{\text{eff}} + \alpha \left( \vec{M} \times \frac{\partial \vec{M}}{\partial t} \right) \quad (2)$$

where  $\mu_0$  is the permeability of free space,  $\gamma$  is the Gilbert gyromagnetic ratio,  $\alpha$  is the Gilbert damping constant, and  $\vec{M}$  is the normalized magnetization vector. The effective magnetic field,  $\vec{H}_{\text{eff}}$ , includes contributions from the external field ( $\vec{H}_{\text{ext}}$ ), exchange field ( $\vec{H}_{\text{ex}}$ ), demagnetization field ( $\vec{H}_{\text{d}}$ ), magnetocrystalline anisotropy field ( $\vec{H}_{\text{anis}}$ ), and magnetoelastic field ( $\vec{H}_{\text{me}}$ ) effects.

The quasi-static Ampere's law is  $\vec{H}_{\text{d}} = -\nabla \phi_m$ , where  $\vec{H}_{\text{d}}$  is the demagnetization field vector and  $\phi_m$  is the magnetic potential. This factor contributes significantly to the dipole–dipole coupling and the effective field in the LLG equation. Combining this equation with the divergence

of magnetic induction equal to zero and the constitutive relation,  $\vec{B} = \mu_0(\vec{H} + \vec{M})$ , produces an equation for  $\phi_m$  in terms of the magnetization  $\vec{M}$ . The magnetization couples with the effective magnetic field through this demagnetization term. Furthermore, substituting the constitutive relations into the elasto–dynamics and LLG equations produces a cross-coupled set of nonlinear equations relating the displacements, the magnetization, and the magnetic potential as follows:

$$\rho \frac{\partial^2 \vec{u}}{\partial t^2} - \nabla \cdot \mathbf{C} \left[ \frac{1}{2} (\nabla \vec{u} + (\nabla \vec{u})^T) \right] + \nabla \cdot \mathbf{C} (\lambda^M \vec{M} \vec{M}^T) = \vec{0} \quad (3)$$

$$\frac{\partial \vec{M}}{\partial t} = -\mu_0 \gamma (\vec{M} \times (\vec{H}_{\text{ext}} + \vec{H}_{\text{ex}}(\vec{M}) + \vec{H}_{\text{d}}(\phi_m) + \vec{H}_{\text{anis}}(\vec{M}) + \vec{H}_{\text{me}}(\vec{M}, \vec{u}))) + \alpha \left( \vec{M} \times \frac{\partial \vec{M}}{\partial t} \right) \quad (4)$$

$$\nabla^2 \phi_m = M_s (\nabla \cdot \vec{m}) \quad (5)$$

where  $\mathbf{C}$  is the stiffness tensor and  $\lambda^M$  is the magnetostriction tensor.

In a fashion similar to that of the magnetic potential, the quasi-static Faraday's law implies that  $\vec{E} = -\nabla \phi_E$ , where  $\vec{E}$  is the electric field and  $\phi_E$  is the electric potential. This equation coupled with Gauss's Law and a proper constitutive form provides for piezoelectric coupling within the model. COMSOL is used to solve the weak form of these systems of partial differential equations. This multiphysics solution produces pointwise values for the mechanical displacement, electric potential, magnetic potential, and magnetization throughout the PMN–PT substrate and Ni rings.

**Conflict of Interest:** The authors declare no competing financial interest.

**Acknowledgment.** Samples were prepared by H.S. PEEM experiments were performed by H.S., M.E.N., J.L.H., M.A.M., A.D., and A.Y. Coupled micromagnetic/elastodynamic simulations were performed by C.-y. L. and S.K. Strain measurements were performed by H.S. and K.W. Magnetic microbead experiments were carried out by M.E.N. and B.M.M. OOMMF micromagnetic simulations were performed by H.S. and B.M.M. The experiments were conceived by R.C., G.P.C., J.B., M.K., and M.E.N. The manuscript was written by M.E.N., H.S., C.-y. L., S.K., and R.C. The authors would like to thank A. Scholl for additional assistance at the PEEM end station of the Advanced Light Source. We also thank J. Clarkson and R. Ramesh for sample characterization assistance. We also acknowledge the use of the fabrication facility at the Integrated Systems Nanofabrication Cleanroom at the California NanoSystems Institute. We gratefully acknowledge support from the National Science Foundation through the Cooperative Agreement Award EEC-1160504 for Solicitation NSF 11-537 (TANMS) and the NSF Center for Energy Efficient Electronics Science. The work at the Advanced Light Source at Lawrence Berkeley National Laboratory is supported by the Director, Office of Science, Office of Basic Energy Sciences, U.S. Department of Energy, under contract number DE-AC02-05CH11231. The work in Mainz is supported by the EU (IFOX NMP3-LA-2010 246102) and the DFG.

**Supporting Information Available:** Additional micromagnetic/elastodynamic simulations that explain the shear lag in our structures, piezo-response force microscopy images of the domain structure in the PMN–PT substrates, XMCD-PEEM images and analysis of electrically driven strain control in a magnetic disk, a simple magnetoelastic model that describes the domain reorientation, and an OOMMF-based model that calculates the magneto-static coupling forces between rings and SPMs as a function of bead sizes and ring geometries. Also included are five videos; the first two show XMCD-PEEM images of the magnetic rings as a function of voltage during the poling and depoling process, the third is a simulation of the poling and depoling process calculated using the micromagnetic/elastodynamic model, and the final two videos show that SPMs magnetically coupled to DWs move upon

the application of an electric field. The Supporting Information is available free of charge on the ACS Publications website at DOI: 10.1021/nn5056332.

## REFERENCES AND NOTES

- Chu, Y.-H.; Martin, L. W.; Holcomb, M. B.; Gajek, M.; Han, S.-J.; He, Q.; Balke, N.; Yang, C.-H.; Lee, D.; Hu, W. Electric-Field Control of Local Ferromagnetism Using a Magneto-electric Multiferroic. *Nat. Mater.* **2008**, *7*, 478–482.
- Heron, J.; Trassin, M.; Ashraf, K.; Gajek, M.; He, Q.; Yang, S.; Nikonov, D.; Chu, Y.; Salahuddin, S.; Ramesh, R. Electric-Field-Induced Magnetization Reversal in a Ferromagnet-Multiferroic Heterostructure. *Phys. Rev. Lett.* **2011**, *107*, 217202.
- Novosad, V.; Otani, Y.; Ohsawa, A.; Kim, S.; Fukamichi, K.; Koike, J.; Maruyama, K.; Kitakami, O.; Shimada, Y. Novel Magnetostrictive Memory Device. *J. Appl. Phys.* **2000**, *87*, 6400–6402.
- Lee, J.-W.; Shin, S.-C.; Kim, S.-K. Spin Engineering of CoPd Alloy Films Via the Inverse Piezoelectric Effect. *Appl. Phys. Lett.* **2003**, *82*, 2458–2460.
- Lahtinen, T. H. E.; Franke, K. J. A.; van Dijken, S. Electric-Field Control of Magnetic Domain Wall Motion and Local Magnetization Reversal. *Sci. Rep.* **2012**, *2*, 258.
- Ralph, D.; Stiles, M. D. Spin Transfer Torques. *J. Magn. Magn. Mater.* **2008**, *320*, 1190–1216.
- Parkin, S. S.; Hayashi, M.; Thomas, L. Magnetic Domain-Wall Racetrack Memory. *Science* **2008**, *320*, 190–194.
- Åkerman, J. Toward a Universal Memory. *Science* **2005**, *308*, 508–510.
- Lei, N.; Devolder, T.; Agnus, G.; Aubert, P.; Daniel, L.; Kim, J. V.; Zhao, W.; Trypiniotis, T.; Cowburn, R. P.; Chappert, C.; et al. Strain-Controlled Magnetic Domain Wall Propagation in Hybrid Piezoelectric/Ferromagnetic Structures. *Nat. Commun.* **2013**, *4*, 1378.
- Fashami, M. S.; Atulasimha, J.; Bandyopadhyay, S. Magnetization Dynamics, Throughput and Energy Dissipation in a Universal Multiferroic Nanomagnetic Logic Gate with Fan-in and Fan-Out. *Nanotechnology* **2012**, *23*, 105201.
- Lee, J.-H.; Jang, J.-t.; Choi, J.-s.; Moon, S. H.; Noh, S.-H.; Kim, J.-w.; Kim, J.-G.; Kim, I.-S.; Park, K. I.; Cheon, J. Exchange-Coupled Magnetic Nanoparticles for Efficient Heat Induction. *Nat. Nanotechnol.* **2011**, *6*, 418–422.
- Nair, M.; Guduru, R.; Liang, P.; Hong, J.; Sagar, V.; Khizroev, S. Externally Controlled On-Demand Release of Anti-HIV Drug Using Magneto-Electric Nanoparticles as Carriers. *Nat. Commun.* **2013**, *4*, 1707.
- Rapoport, E.; Beach, G. S. Dynamics of Superparamagnetic Microbead Transport Along Magnetic Nanotracks by Magnetic Domain Walls. *Appl. Phys. Lett.* **2012**, *100*, 082401.
- Rapoport, E.; Beach, G. Transport Dynamics of Superparamagnetic Microbeads Trapped by Mobile Magnetic Domain Walls. *Phys. Rev. B* **2013**, *87*, 174426.
- Conroy, R. S.; Zabow, G.; Moreland, J.; Koretsky, A. P. Controlled Transport of Magnetic Particles Using Soft Magnetic Patterns. *Appl. Phys. Lett.* **2008**, *93*, 203901.
- Vieira, G.; Henighan, T.; Chen, A.; Hauser, A. J.; Yang, F. Y.; Chalmers, J. J.; Sooryakumar, R. Magnetic Wire Traps and Programmable Manipulation of Biological Cells. *Phys. Rev. Lett.* **2009**, *103*, 128101.
- Sarella, A.; Torti, A.; Donolato, M.; Pancaldi, M.; Vavassori, P. Two-Dimensional Programmable Manipulation of Magnetic Nanoparticles on-Chip. *Adv. Mater.* **2014**, *26*, 2384–2390.
- Khalil, I. S.; Dijkslag, H. C.; Abelman, L.; Misra, S. Magnetosperm: A Microrobot That Navigates Using Weak Magnetic Fields. *Appl. Phys. Lett.* **2014**, *104*, 223701.
- Gao, W.; Feng, X.; Pei, A.; Kane, C. R.; Tam, R.; Hennessy, C.; Wang, J. Bioinspired Helical Microswimmers Based on Vascular Plants. *Nano Lett.* **2013**, *14*, 305–310.
- Ramesh, R.; Spaldin, N. A. Multiferroics: Progress and Prospects in Thin Films. *Nat. Mater.* **2007**, *6*, 21–29.
- Hockel, J. L.; Bur, A.; Wu, T.; Wetzlar, K. P.; Carman, G. P. Electric Field Induced Magnetization Rotation in Patterned Ni Ring/Pb(Mg<sub>1/3</sub>Nb<sub>2/3</sub>)O<sub>3</sub>[(1–0.32)-[PbTiO<sub>3</sub>]<sub>0.32</sub>] Heterostructures. *Appl. Phys. Lett.* **2012**, *100*, 022401.
- Ashkin, A.; Dziedzic, J.; Bjorkholm, J.; Chu, S. Observation of a Single-Beam Gradient Force Optical Trap for Dielectric Particles. *Opt. Lett.* **1986**, *11*, 288–290.
- Grier, D. G. A Revolution in Optical Manipulation. *Nature* **2003**, *424*, 810–816.
- Fan, D.; Cammarata, R.; Chien, C. Precision Transport and Assembling of Nanowires in Suspension by Electric Fields. *Appl. Phys. Lett.* **2008**, *92*, 093115.
- Ding, X.; Li, P.; Lin, S.-C. S.; Stratton, Z. S.; Nama, N.; Guo, F.; Slotcavage, D.; Mao, X.; Shi, J.; Costanzo, F. Surface Acoustic Wave Microfluidics. *Lab Chip* **2013**, *13*, 3626–3649.
- Hansen, P. M.; Bhatia, V. K.; Harrit, N.; Oddershede, L. Expanding the Optical Trapping Range of Gold Nanoparticles. *Nano Lett.* **2005**, *5*, 1937–1942.
- Min, C.; Shen, Z.; Shen, J.; Zhang, Y.; Fang, H.; Yuan, G.; Du, L.; Zhu, S.; Lei, T.; Yuan, X. Focused Plasmonic Trapping of Metallic Particles. *Nat. Commun.* **2013**, *4*, 2891.
- Wang, M. D.; Yin, H.; Landick, R.; Gelles, J.; Block, S. M. Stretching DNA with Optical Tweezers. *Biophys. J.* **1997**, *72*, 1335–1346.
- Min, T. L.; Mears, P. J.; Chubiz, L. M.; Rao, C. V.; Golding, I.; Chemla, Y. R. High-Resolution, Long-Term Characterization of Bacterial Motility Using Optical Tweezers. *Nat. Methods* **2009**, *6*, 831–835.
- Righini, M.; Ghenuche, P.; Cherukulappurath, S.; Myroshnychenko, V.; García de Abajo, F. J.; Quidant, R. Nano-optical Trapping of Rayleigh Particles and *Escherichia coli* Bacteria with Resonant Optical Antennas. *Nano Lett.* **2009**, *9*, 3387–3391.
- Rothman, J.; Kläui, M.; Lopez-Diaz, L.; Vaz, C.; Bleloch, A.; Bland, J.; Cui, Z.; Speaks, R. Observation of a Bi-Domain State and Nucleation Free Switching in Mesoscopic Ring Magnets. *Phys. Rev. Lett.* **2001**, *86*, 1098.
- O'Handley, R. C. *Modern Magnetic Materials: Principles and Applications*; Wiley: New York, 1999; p 221.
- Doran, A.; Church, M.; Miller, T.; Morrison, G.; Young, A. T.; Scholl, A. Cryogenic PEEM at the Advanced Light Source. *J. Electron Spectrosc. Relat. Phenom.* **2012**, *185*, 340–346.
- Chen, C.; Sette, F.; Ma, Y.; Modesti, S. Soft-X-Ray Magnetic Circular Dichroism at the L<sub>2,3</sub> Edges of Nickel. *Phys. Rev. B* **1990**, *42*, 7262.
- Liang, C.-y.; Keller, S. M.; Sepulveda, A. E.; Bur, A.; Sun, W.-Y.; Wetzlar, K.; Carman, G. P. Modeling of Magnetoelastic Nanostructures with a Fully Coupled Mechanical-Micromagnetic Model. *Nanotechnology* **2014**, *25*, 435701.
- Donahue, M.; Porter, D. *Oomf User's Guide*, version 1.0; Interagency Report NISTIR 6376; National Institute of Standards and Technology: Gaithersburg, MD, 1999.
- Kläui, M.; Vaz, C.; Lopez-Diaz, L.; Bland, J. Vortex Formation in Narrow Ferromagnetic Rings. *J. Phys.: Condens. Matter* **2003**, *15*, R985.
- Laufenberg, M.; Backes, D.; Bühner, W.; Bedau, D.; Kläui, M.; Rüdiger, U.; Vaz, C. A.; Bland, J. A. C.; Heyderman, L. J.; Nolting, F. Observation of Thermally Activated Domain Wall Transformations. *Appl. Phys. Lett.* **2006**, *88*, 052507.
- McMichael, R. D.; Donahue, M. J. Head to Head Domain Wall Structures in Thin Magnetic Strips. *IEEE Trans. Magn.* **1997**, *33*, 4167–4169.
- Wu, T.; Zhao, P.; Bao, M.; Bur, A.; Hockel, J. L.; Wong, K.; Mohanchandra, K. P.; Lynch, C. S.; Carman, G. P. Domain Engineered Switchable Strain States in Ferroelectric (011) [Pb(Mg<sub>1/3</sub>Nb<sub>2/3</sub>)O<sub>3</sub>]<sub>(1-x)</sub>-[PbTiO<sub>3</sub>]<sub>x</sub> (PMN-PT, X≈0.32) Single Crystals. *J. Appl. Phys.* **2011**, *109*, 124101.
- Weiler, M.; Brandlmaier, A.; Geprägs, S.; Althammer, M.; Opel, M.; Bihler, C.; Huebl, H.; Brandt, M.; Gross, R.; Goennenwein, S. Voltage Controlled Inversion of Magnetic Anisotropy in a Ferromagnetic Thin Film at Room Temperature. *New J. Phys.* **2009**, *11*, 013021.
- Buzzi, M.; Chopdekar, R.; Hockel, J.; Bur, A.; Wu, T.; Pilet, N.; Warnicke, P.; Carman, G.; Heyderman, L.; Nolting, F. Single Domain Spin Manipulation by Electric Fields in Strain

- Coupled Artificial Multiferroic Nanostructures. *Phys. Rev. Lett.* **2013**, *111*, 027204.
43. Choi, S. W.; Shrout, R. T.; Jang, S. J.; Bhalla, A. S. Morphotropic Phase Boundary in  $\text{Pb}(\text{Mg}_{1/3}\text{Nb}_{2/3})\text{O}_3\text{-PbTiO}_3$  System. *Mater. Lett.* **1989**, *8*, 253–255.
  44. Chang, C.-M.; Carman, G. P. Experimental Evidence of End Effects in Magneto-Electric Laminate Composites. *J. Appl. Phys.* **2007**, *102*, 124901.
  45. Chang, C.-M.; Carman, G. P. Modeling Shear Lag and Demagnetization Effects in Magneto-Electric Laminate Composites. *Phys. Rev. B* **2007**, *76*, 134116.
  46. Stöhr, J.; Siegmann, H. C. *Magnetism: From Fundamentals to Nanoscale Dynamics*; Springer: Berlin, 2006; p 441.
  47. Park, S.-E.; Shrout, T. R. Ultrahigh Strain and Piezoelectric Behavior in Relaxor Based Ferroelectric Single Crystals. *J. Appl. Phys.* **1997**, *82*, 1804–1811.
  48. Bryan, M. T.; Dean, J.; Schrefl, T.; Thompson, F. E.; Haycock, J.; Allwood, D. A. The Effect of Trapping Superparamagnetic Beads on Domain Wall Motion. *Appl. Phys. Lett.* **2010**, *96*, 192503.
  49. Cui, J.; Hockel, J. L.; Nordeen, P. K.; Pisani, D. M.; Liang, C.-y.; Carman, G. P.; Lynch, C. S. A Method to Control Magnetism in Individual Strain-Mediated Magnetoelectric Islands. *Appl. Phys. Lett.* **2013**, *103*, 232905.